research papers

(U)SAXS characterization of porous microstructure of chert: insights into organic matter preservation

Patricio Munoz,[a]* Jan Ilavsky,[b]* Matthew Newville,[c] Niklaus U. Wetter,[d] Rafael André Lourenço,[e] Marcelo Barbosa de Andrade,[f,g] Tereza S. Martins,[h] Jessica Dipold,[d] Anderson Z. Freitas,[d] Luis Carlos Cides da Silva[i] and Cristiano Luis Pinto Oliveira[i]
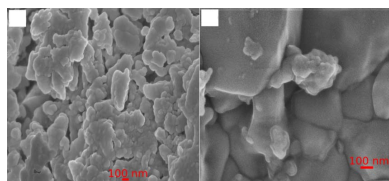
[a]Institute of Geosciences (IGc-USP), University of São Paulo, Rua do Lago 562, São Paulo, SP 05508080, Brazil, [b]Argonne National Laboratory, 9700 S Cass Avenue, Argonne, IL 60439, USA, [c]Center for Advanced Radiation Sources, University of Chicago, Chicago, Illinois 60637, USA, [d]Nuclear and Energy Research Institute (IPEN-CNEN), Avenida Professor Lineu Prestes 2242, São Paulo, SP 05508000, Brazil, [e]Institute of Oceanography (IOUSP), University of São Paulo, Praça do Oceanografico 191, São Paulo, SP 05508900, Brazil, [f]Sao Carlos Institute of Physics, University of São Paulo (IFSC-USP), Avenida Trabalhador São-Carlense 400 – Caixa Postal 369, Sao Carlos, SP 13560-970, Brazil, [g]Physics Department, Federal University of Ouro Preto, Ouro Preto, MG 35400-000, Brazil, [h]Department of Chemistry, Federal University of São Paulo (UNIFESP), Rua Sao Nicolau 210, Diadema, SP 09913030, Brazil, and [i]Institute of Physics (IFUSP), University of São Paulo, Rua do Matão 187, São Paulo, SP 05314-970, Brazil. *Correspondence e-mail: patricio.m.munoz@usp.br, ilavsky@aps.anl.gov

This study characterizes the microstructure and mineralogy of 132 (ODP sample), 1000 and 1880 million-year-old chert samples. By using ultra-small-angle X-ray scattering (USAXS), wide-angle X-ray scattering and other techniques, the preservation of organic matter (OM) in these samples is studied. The scarce microstructural data reported on chert contrast with many studies addressing porosity evolution in other sedimentary rocks. The aim of this work is to solve the distribution of OM and silica in chert by characterizing samples before and after combustion to pinpoint the OM distribution inside the porous silica matrix. The samples are predominantly composed of alpha quartz and show increasing crystallite sizes up to 33 ± 5 nm (1σ standard deviation or SD). In older samples, low water abundances ($\sim 0.03\%$) suggest progressive dehydration. (U)SAXS data reveal a porous matrix that evolves over geological time, including, from younger to older samples, (1) a decreasing pore volume down to 1%, (2) greater pore sizes hosting OM, (3) decreasing specific surface area values from younger (9.3 ± 0.1 m^2 g^{-1}) to older samples (0.63 ± 0.07 m^2 g^{-1}, 1σ SD) and (4) a lower background intensity correlated to decreasing hydrogen abundances. The pore-volume distributions (PVDs) show that pores ranging from 4 to 100 nm accumulate the greater volume fraction of OM. Raman data show aromatic organic clusters up to 20 nm in older samples. Raman and PVD data suggest that OM is located mostly in mesopores. Observed structural changes, silica–OM interactions and the hydrophobicity of the OM could explain the OM preservation in chert.

1. Introduction

The characterization of sedimentary rock microstructure has permitted an understanding of the transport, migration and retention of fluids in Earth's crust. The microstructure of sedimentary rock comprises several components: mineral grains, amorphous phases, pores, rock fragments, microfractures and internal planar boundaries. To become a rock, a sedimentary deposit experiences compaction by burial, dissolution and precipitation of new mineral phases. Then, the evolution of its microstructure over time arises from these sedimentary-rock-forming processes (*e.g.* Anovitz *et al.*, 2013).

Sandstones and shales (*i.e.* clastic sedimentary rocks) host a significant part of hydrocarbon reserves. As such, they have

been extensively studied (*e.g.* Scherer, 1987; Anovitz & Cole, 2015). These studies outlined that first-order parameters controlling porosity include compaction, age, quartz content and particle-size distribution standard deviation (SD) (Scherer, 1987). Meanwhile, dissolution, precipitation and depth-related temperature are second-order parameters controlling porosity (Scherer, 1987; Taylor *et al.*, 2010).

Clastic sedimentary rocks could be equivalent to granular media modified by compaction under confinement. Compaction induces modifications in the porous matrix simultaneous to changes in particle morphology (Chester *et al.*, 2004; Marks *et al.*, 2015). Pressure (or depth of burial confinement) could be a primary controlling factor in porosity.

However, a critical analysis by Anovitz & Cole (2019) of 47 small-angle scattering (SAS) papers demonstrated that the modification of porous microstructure of clastic sedimentary rocks depends on several additional factors, including abundance of organics, type of organic matter (OM) and carbonatization (maturation) of OM. Geological time could also be a primary factor controlling porosity because time and temperature control the evolution of the chemistry and structure of OM preserved in sedimentary rocks (Alleon & Summons, 2019). These findings support that silica particles and their porous network evolve in time and space inside clastic sedimentary rocks (Anovitz *et al.*, 2013).

Cherts are quartz microaggregates formed by compaction and dissolution–precipitation processes acting on silica deposits (*i.e.* silica diagenesis). All SAS analyses reviewed by Anovitz & Cole (2019) were collected from sedimentary samples of lesser stiffness and average elastic modulus than those exhibited by quartz. Thus, cherts could not have a significant porosity variation according to depth in silica-rich deposits because of quartz's high stiffness and very low compressibility.

Silica diagenesis is a highly complex compaction and dissolution–precipitation process driven by transformations of SiO_2 amorphous phases to quartz (*e.g.* Stein & Kirkpatrick, 1976; Williams *et al.*, 1985; Chaika & Williams, 2001; Wrona *et al.*, 2015, 2017). Parameters that control these transformations include burial time, pressure, temperature, pH of the solvent, particle surface area, solubility, host-rock lithology and content of OM (Williams *et al.*, 1985; Hinman, 1990; Wrona *et al.*, 2017). Williams *et al.* (1985) suggested that solubility and surface area are the predominant factors controlling the porosity and permeability of silica-rich sedimentary rocks. Furthermore, solubility exhibits a nonlinear behavior affecting silica diagenesis via dissolution, mostly in nanometric pores, and favoring silica precipitation in pores greater than 8 µm (Emmanuel & Ague, 2009). These studies reveal that silica diagenesis induces structural and chemical heterogeneities observable at a nano- and micro-metric scale in chert.

Physicochemical and microstructural parameters such as porosity, pore size, particle surface area, solubility and OM content are local spatially variable parameters controlling silica diagenesis (*e.g.* Stein & Kirkpatrick, 1976; Williams *et al.*, 1985; Chaika & Williams, 2001; Wrona *et al.*, 2015, 2017; Anovitz & Cole, 2019). Thus, the characterization and analysis

of these microstructural features of chert offer a bridge to understanding silica diagenesis in time.

The common evolutive starting point for chert samples is their homogenous chemical and almost monomineralic composition. In parallel, the geological age of chert samples depicts a simple reality: older samples experience greater time intervals of burial and, therefore, greater silica diagenesis progression. Thus, we present an extensive microstructural and chemical characterization of cherts of different geological ages spanning a time interval from 132 to 1880 million years (Ma).

Several studies have suggested a diversity of tectonic settings for sedimentary rocks. For example, for the ∼1880 million-year-old Gunflint Formation, at least two contrasting tectonic settings have been proposed (*e.g.* Fralick *et al.*, 2002). Similarly, the success of inference of tectonic setting based on geochemical data varies between 0 and ∼60% for young marine sedimentary rocks (*e.g.* Armstrong-Altrin & Verma, 2005). This fact reinforces the characterization of microstructure as critical information to understand the forming processes of chert.

Our approach exploits the little microstructural data previously reported for chert samples. Most transmission electron microscopy images show the occurrence of OM inside the chert pore network (Moreau & Sharp, 2004; Wacey *et al.*, 2013; Natalio *et al.*, 2021). Graetsch & Ibel (1997) reported the first and sole previous small-angle neutron scattering data collected on chert.

Chert-forming processes induce porosity reduction, dehydration of amorphous silica and the crystallization of more stable SiO_2 polymorphs (Williams *et al.*, 1985). The scarcity of chert microstructural data has hindered understanding of the spatial relationship between chert's silica matrix and OM.

Ultra-small-angle X-ray scattering (USAXS) is a powerful tool to quantify microstructural key parameters in rocks, which can characterize an entire pore population across several decades in size (*e.g.* Radlinski *et al.*, 2004; Anovitz *et al.*, 2013). Specifically, pore size, volume distribution and pore connectivity are critical parameters to address the issue of OM preservation in chert.

Previous SAS characterization of sandstones and shales yielded complex scattering profiles. For example, the geometry of these profiles included subtle horizontal steps, subcurves, down concavities and points where the power-law slope changes (*e.g.* Anovitz *et al.*, 2013; Bahadur *et al.*, 2014; Anovitz & Cole, 2019). This complexity of the scattering profile makes the fractal approach used to infer how a porous matrix arranges in space (McCarthy *et al.*, 2008) somewhat challenging to use.

Sandstones and shales are polymineralic in composition, which induces significant variation in density and X-ray scattering length density (SLD). In conjunction with OM occurrences, this limits the validity of their modeling as two-phase systems, as is typically done. On the other hand, cherts are closer to a two-phase system, given their almost monomineralic compositions.

In this work, we have characterized the microstructure of differently aged cherts to gain a picture of the evolution of

silica microstructure over geological time. We have used combustion to remove OM from the pores to gain insights into the location of OM and the silica matrix. By collecting (U)SAXS data from intact and combusted samples and results from other techniques, we evaluate both pore size and OM size distributions. These results contribute to understanding the relationship between porosity, pore-size distribution, specific surface area (SSA) and relevant geochemical parameters in chert.

2. Methodology

Three chert samples of different ages were studied. A Cretaceous sample (S1, 132 Ma) was collected from oceanic environments near Japan by the Ocean Drilling Program (Plank *et al.*, 2000). Two older samples, S51 and S52, were collected from continental settings. Sample S52, with an estimated age of ~1000 Ma, was collected from the Narssârssuk Formation, Greenland (Strother *et al.*, 1983). Sample S51 was collected from the northern border of Lake Superior and corresponds to a stromatolitic chert with an estimated age of ~1880 Ma (Barghoorn & Tyler, 1965; Fralick *et al.*, 2002).

We have applied a broad range of characterization techniques: gas chromatography with a mass spectrometer (GC–MS) and a flame ionization detector (GC–FID), Raman microspectroscopy, thermogravimetric analysis (TGA), N_2 sorption, CHN (carbon, hydrogen and nitrogen) elemental analysis, field-emission scanning electron microscopy (FESEM), USAXS, SAXS, wide-angle X-ray scattering (WAXS), and micro-X-ray fluorescence mapping (μXRF). (U)SAXS and WAXS experimental details are explained here due to their high relevance to the issue treated in this article. The appendices provide details of the other analytical techniques. Data collected by using WAXS (in combusted samples), Raman microspectroscopy, TGA, μXRF, GC–MS and GC–FID, CHN elemental analysis, and N_2 sorption are reported in the supporting information.

2.1. USAXS, SAXS and WAXS experiments and analysis

Millimetric samples were split into two fragments and then polished to achieve micrometric thicknesses. One fragment was maintained intact (NB: non-burned), while the other was combusted (B: burned) for 2 h using a gradient of $10°C \, min^{-1}$ under air atmosphere (Appendix *B*1). Combusted samples were exposed for less than 5 min to the final temperature (1000°C). This combustion procedure released most of the OM from the porous matrix. Then, the samples were mounted between two Kapton foils and fixed with Scotch tape into a paper frame for handling.

Initial SAXS/WAXS experiments were performed using Cu and Mo sources at the Institute of Physics University of Sao Paulo (IFUSP) on a Xeuss 2.0 instrument (Xenocs). This instrument yields an X-ray photon flux of ~$0.5 \times 10^8 \, mm^{-2} \, s^{-1}$. The X-ray beam was ~700 μm. The combined *q* range is between 0.05 and ~0.2 $Å^{-1}$; here, $q = 4\pi/\lambda \sin(\theta)$, where λ is the wavelength and θ is half of the scattering angle. Data were reduced using in-house software (*SuperSAXS*, Dr

C. Oliveira). To estimate the sample's thickness, we used the Lambert–Beer law $Tm = \exp(-\mu t)$, where Tm is the measured transmission, μ is the linear X-ray attenuation coefficient of the sample and *t* is the estimated sample thickness.

Absolutely calibrated USAXS, SAXS and WAXS experiments were performed at the 9-ID beamline using the USAXS instrument at the Advanced Photon Source (APS), Argonne National Laboratory (Ilavsky *et al.*, 2009, 2013). The combined *q* range is between 1×10^{-4} and ~5.86 $Å^{-1}$. The X-ray energy was 21 keV (λ = 0.590401 Å). The X-ray photon flux was ~$5 \times 10^{12} \, mm^{-2} \, s^{-1}$. The combined USAXS/SAXS/WAXS measurement data-collection time was ~5 min. The X-ray beam was 800 and 200 μm for combusted and intact samples, respectively. Data were reduced using *Nika* (Ilavsky, 2012) and were put on an absolute intensity scale.

The thickness varied between 130 and 300 μm, which resulted in sample X-ray transmissions of at least 90% for APS experiments. Experiments at IFUSP had a minimum sample transmission of ~50%. We focused our analysis on (U)SAXS data using the pore-volume distribution (PVD) approach, given the microstructural complexities reported in sedimentary rocks (Anovitz *et al.*, 2013; Bahadur *et al.*, 2014; Anovitz & Cole, 2019).

2.1.1. Analysis of (U)SAXS profiles: size distribution of the pore volume. Analysis of (U)SAXS profiles focused on the calculation of size distribution of pore volume, total volume fraction (TVF), surface area, power-law slope and aspect ratio. These microstructural features were estimated by fitting physical models that assume a dilute limit model for the pore network (McCarthy *et al.*, 2008), which depends on assumptions about the homogeneity of particle composition and the scatterers' shape. Thus, the results are model dependent, and other independent analytical techniques are needed to validate the assumptions of the models used for (U)SAXS analysis.

In our PVD calculations, we used (1) the maximum entropy method and (2) the invariant $Q_{inv} = 2\pi^2 \emptyset (1 - \emptyset) \Delta\rho^2$ that corresponds to the integral of the Kratky transform. The maximum entropy method is available in the *Irena* software (Ilavsky & Jemian, 2009). This method assumes that all particles are the same shape; all particles have the same contrast, no structure factor and a low volume fraction ($\emptyset$). A low volume fraction ensures that the contrast is $|\Delta\rho|^2 = (\rho_{sil} - \rho_{air})^2$ because this physical quantity is inversely proportional to $\emptyset(1 - \emptyset)$. ρ_{sil} and ρ_{air} denote the X-ray SLDs for silica and air, respectively. We used a ρ_{sil} of $22.45 \times 10^{-10} \, cm^{-2}$ and a ρ_{air} of $1 \times 10^2 \, cm^{-2}$.

In these complex systems, we need to verify that the microstructure can be approximated as a two-phase system. Assuming that the silica phase is chemically homogeneous, the contrast is $|\Delta\rho|^2 = (\rho_{sil} - \rho_{air})^2$, and the scattering intensity [$I(q)$] is expressed by equation (1) (Kotzias *et al.*, 1987; McCarthy *et al.*, 2008):

$$I(q) = |\Delta\rho|^2 \int_0^\infty |F(q,r)|^2 V(r)^2 NP(r) \, dr, \qquad (1)$$

where $|F(q, r)|^2$ corresponds to the form factor, $V(r)$ is the particle volume, N is the total number of scatterers and $P(r)$ is the probability of occurrence of scatterers at size r (Ilavsky, 2021).

In our PVD calculations, we used a sphere form factor to simplify calculations and an X-ray SLD (ρ_{sil}) of 22.45×10^{10} cm^{-2}, which is a typical value for SiO$_2$ polymorphs. We used the same contrast for combusted and intact samples considering $\rho_{air} \simeq 0$. The q range varies from 3×10^{-4} to ~ 0.2 Å^{-1} for most PVD-fitting calculations.

The invariant $Q_{inv} = \int_0^\infty q^2 I(q) \, dq = 2\pi^2 \emptyset (1 - \emptyset) \Delta \rho^2$ provides an independent method to measure the porosity ($\emptyset$) of the scatterer's phase. This quantity is estimated using scattering data from a similar q range to those used to estimate PVDs. Additionally, a background composed of a power law plus a flat $I(q)_0$ value was subtracted using *Irena*.

Using the invariant formulation and equations from McCarthy *et al.* (2008), we estimated the SLD for OM (ρ_{OM}) in our samples. First, we calculated the subtraction of the invariant for the intact sample (Q_{inv}^{NB}) from that for the combusted sample (Q_{inv}^{B}). This subtraction is

$$Q_{inv}^{B} - Q_{inv}^{NB} \simeq 2\pi^2 \left(\emptyset_B^2 |\Delta \rho|_B^2 - \emptyset_{NB}^2 |\Delta \rho|_{NB}^2 \right). \quad (2)$$

Thus, inputs from invariants, porosities and contrast for quartz permitted us to calculate the contrast for intact samples ($|\Delta \rho|_{NB}^2$). This calculation is possible given that $(Q_{inv}^{B} - Q_{inv}^{NB})/2\pi^2 < \emptyset_B^2 |\Delta \rho|_B^2$. Equation (7) of McCarthy *et al.* (2008) defined this contrast as $|\Delta \rho|_{NB}^2 = (\rho_{mineral} - \rho_{OM})^2$, permitting an estimation of SLD for OM. The results of these calculations are discussed in Sections 3.2 and 3.6.

All samples yielded similar X-ray transmissions of greater than 90%, suggesting a narrow variation of measured thickness. Consequently, the experimental errors in $I(q)$ are the main source in PVD estimations. The errors in $I(q)$ vary from 3 to 4% for combusted samples and between 6 and 7% for intact samples. These errors determine uncertainties of ~ 8 to ~ 30% in TVF calculated using the maximum entropy method.

Analytical errors in chemical composition are a primary source of error in X-ray SLD and contrast estimations in polymineralic rocks. Therefore, we assessed the homogeneity of mineral composition using WAXS and chemical data. To estimate the external reproducibility of PVDs, we calculated the SD of the average for the individual PVD of each measured point.

2.1.2. Analysis of (U)SAXS profiles: specific surface area.
We calculated SSA values from Porod regions of SAXS profiles via *Irena* macros. Data from the Porod regions were plotted on $q^4 I(q)$ versus q^4 diagrams yielding the Porod constant (C_p) as the intercept of the linear curve $I(q) = C_p/q^4 +$ background (Thomas *et al.*, 1998). Thus, SSA is expressed (in m^2 cm^{-3}) by (Thomas *et al.*, 1998)

$$\frac{S}{V} = \frac{C_p}{2\pi |\Delta \rho|^2}, \quad (3)$$

where S, V and $|\Delta \rho|^2$ stand for surface, volume and contrast, respectively. We used the same contrast for all samples to calculate SSA for combusted samples.

To calculate the S/V ratio outside the Porod regions, we applied a modified version of the formula by Allen (1991) on q regions exhibiting power-law slopes varying between -3 and -4:

$$\left(\frac{S}{V} \right)_r = \left(\frac{S}{V} \right)_0 \left(\frac{r}{r_0} \right)^{-\alpha - 4}. \quad (4)$$

The formula from Allen (1991) applies to pores arranged in surface fractal geometry. That is, tiny pores generate the surface roughness of larger pores [*e.g.* see Fig. 1(*a*) of Allen (1991)]. Extensive difficulties can be found in showing (*i.e.* imaging) such arrangements in rocks. Furthermore, sedimentary rocks yielded SAXS profiles of complex geometries, limiting the fractal approach's application.

SSA measurements could be seriously hampered in rock exhibiting microstructures without a smooth q^{-4} surface. In this regard, Allen's model provides almost a unique tool for such measurement since physisorption methods reproduce discrepant results (*e.g.* Anovitz & Cole, 2019). Thus, we propose to use this modified version of Allen's model [equation (4)] on our intact samples, which exhibited power-law slopes varying between -3 and -4.

In this extension of Allen's model, we also used microstructural data from combusted fragments. $(S/V)_0$ is the ratio calculated from Porod regions of combusted fragments and r_0 indicates the upper limit for the Porod region. The exponent depends on the power-law slope rather than the fractal dimension. In Section 3.6, we assess the applicability of equation (4) in light of the physical meaning of SSA values from intact samples.

2.1.3. WAXS fingerprint of mineral phases: a test of the two-phase condition.
The WAXS profiles were fitted using Lorentzian peaks via *Irena*, yielding values for parameters including d spacing, location on the 2θ scale, width on the 2θ scale [full width at half-maximum (FWHM)], height and area. The conversion from the q scale (Å^{-1}) to angular units (2θ units) was performed in the WAXS fit tool of *Irena*. Section S1 of the supporting information reports values for these parameters in sample S52 (intact and combusted fragment). The crystallite size was estimated using the Scherrer equation and values of these parameters (Section S1). Combustion did not significantly influence the crystallite sizes or other parameters (Section S1). For samples S1 and S51, similar output was obtained.

To identify mineral phases, we compared our WAXS data with the Crystallography Open Database (COD, https://www.crystallography.net/cod/new.html) using the *QualX 2.0* software (Gražulis *et al.*, 2009, 2012; Altomare *et al.*, 2015). The list of peaks located by the software was compared with the COD, yielding a rank based on the figure of merit of fit for each plausible mineral standard.

The differences in the 2θ position are less than 1% between peaks found by *Irena* and *QualX 2.0*, confirming the robustness of the identification procedure. Furthermore, standard mineral phases yielded figure-of-merit values greater than 90%.

Experimental error for intensity is the primary uncertainty source determining errors quantified by the WAXS fit tool in *Irena*. The maximal errors in intensity range from 4 to 6%. Meanwhile, the errors are less than 5% for the height of peaks and less than 1% for peak position.

2.2. Chemical contrast techniques: an additional test of the two-phase condition

In addition to WAXS, we used Raman microspectroscopy and μXRF mapping to survey mineralogical homogeneity at micrometre scales. The μXRF mapping experiments were performed at the 13-ID beamline (APS), and provided chemical images for silicon and most $3d$ transition metals. Such experiments were performed using an energy of 17 keV and an X-ray beam of 2 μm in diameter. Raman data were collected at IPEN-CNEN and IFSC-USP, mainly using a radiation beam ranging from ~1.3 to ~3 μm in diameter. For details, see Appendix *A*1 and Section S2 for μXRF mapping, and Appendix *A*2 and Section S3 for Raman microspectroscopy.

2.3. Other techniques

Appendix *A* contains experimental information on chemical and spectroscopic techniques (μXRF mapping, Raman microspectroscopy, CHN elemental analysis and GC–MS). Appendix *B* outlines TGA and N_2 sorption experiments, while FESEM experiments are detailed in Appendix *C*. Results from these techniques are reported in the supporting information.

3. Results and discussion

3.1. (U)SAXS: variability in scattering intensities and backgrounds

At first glance, the average scattering profiles display complex geometries in double logarithmic q versus $I(q)$ diagrams (Fig. 1). The profiles for intact samples exhibit several regions of changing power-law exponent. Vertical arrows in Fig. 1 highlight these regions. After combustion, all scattering curves show fewer points of change in power-law exponents.

At low and intermediate q, the scattering intensities of combusted samples $[I(q)_B]$ are greater than the intensities of intact samples $[I(q)_{NB}]$ (Fig. 1). For example, the ratio between scattering intensities of intact versus combusted fragments $I(q)_{S1-B}/I(q)_{S1-NB}$ varies from $1.2\times$ to $13\times$ in sample S1. Similar values were calculated in SAXS data from samples S52 and S51 $[I(q)_{S52-B}/I(q)_{S52-NB}$ and $I(q)_{S51-B}/I(q)_{S51-NB}]$. This difference in intensity is expected because a significant proportion of pores originally filled with OM are filled with air after combustion, which increases their scattering strength.

Comparing scattering intensities supports pore-volume differences between combusted samples. For example, the ratio between intensities of samples S1-B and S51-B $[I(q)_{S1-B}/I(q)_{S51-B}]$ varies between $1.2\times$ and $\sim28\times$. Similarly, the ratio of $I(q)_{S52-B}/I(q)_{S51-B}$ varies from $1.2\times$ to $\sim12\times$ at low and

intermediate q ranges. Differences in thickness cannot explain the variability in these ratios (*e.g.* sample S51 is thicker than sample S1). The samples are almost homogenously composed
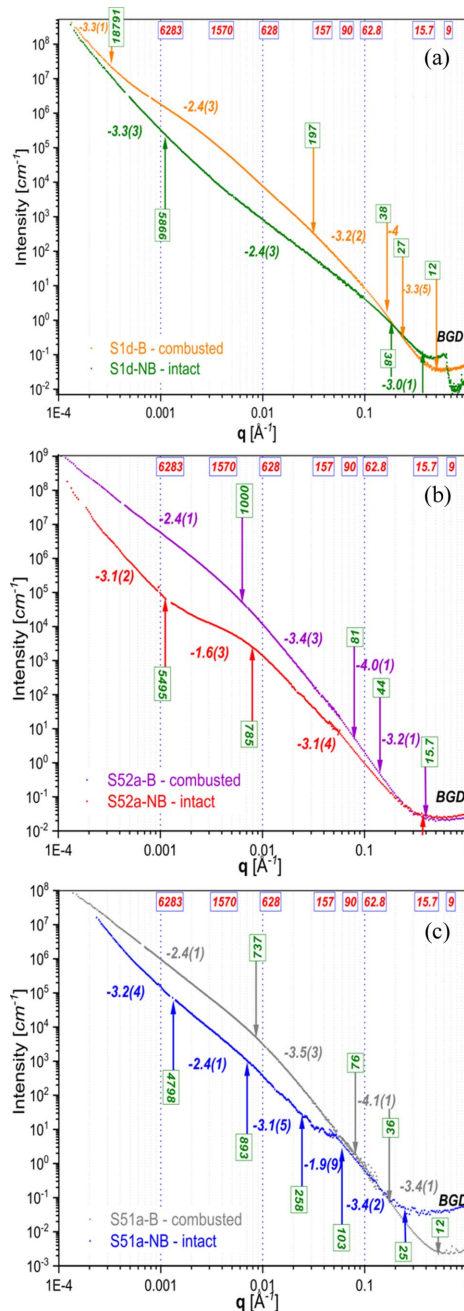
Figure 1
Scattering curves for combusted $[I(q)_B]$ and intact samples $[I(q)_{NB}]$. (*a*) $I(q)$ for sample S1; green and orange denote intact and combusted fragments, respectively. (*b*) $I(q)$ for sample S52; red and violet show intact and combusted fragments, respectively. (*c*) $I(q)$ for sample S51; blue and gray represent intact and combusted fragments, respectively. On each $I(q)$ versus q diagram, the blue upper boxes highlight sizes in ångström calculated using $d = 2\pi/q$, with q values from the abscissa axis. BGD stands for background. Average power-law slope values are displayed in bold italic cases respecting the color codes used for each sample. The number in parentheses highlights the SD (1σ SD) calculated for each average power-law value. Vertical green boxes show scatterer sizes in ångström, representing inflection points where the average power-law slope value changes. For example, Porod regions occur between scatterers with sizes ranging from 44 to 81 Å in combusted sample S52.

of SiO$_2$ polymorphs (see Section 3.2). Thus, this variability is probably due to differences in pore volume among the combusted samples.
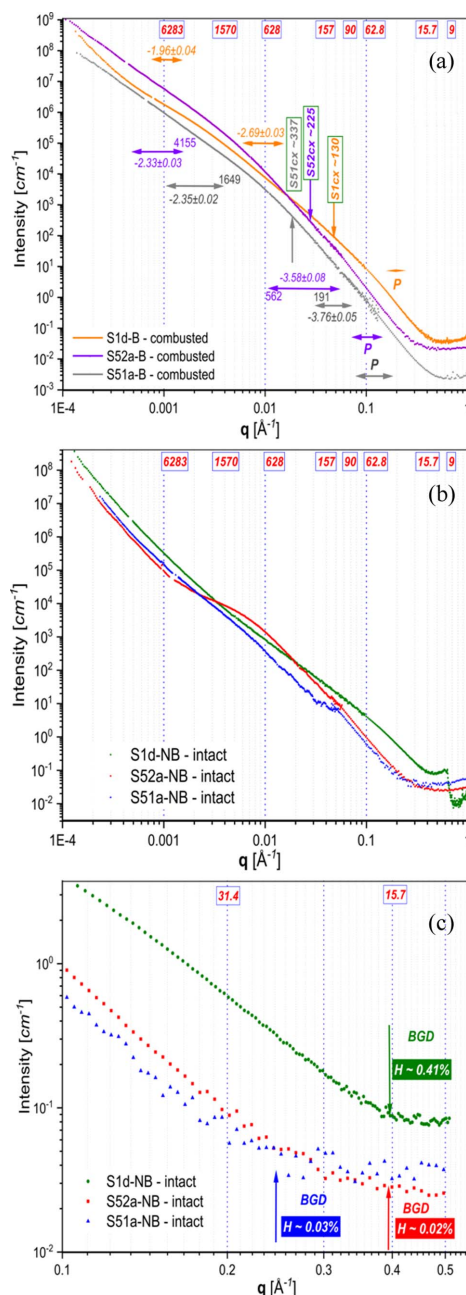
Figure 2
Comparative log–log graphs between scattering curves for (*a*) combusted and (*b*) intact samples. Part (*c*) corresponds to a magnification of Porod and background regions of (*b*). In (*a*), the bidirectional arrows represent segments of constant power-law slopes in scattering curves. Each segment's SD was calculated with 1σ level of statistical significance. The arrows follow the color code used for each sample. The letter 'P' stands for the Porod region. Blue upper boxes highlight sizes in ångström calculated using $d = 2\pi/q$, with q values from the abscissa axis. For each sample, vertical green boxes highlight positions in the q reciprocal space for crystallite sizes (S1cx, S52cx, S51cx) in ångström. In (*c*), the vertical arrows delimit the maximal scatterer sizes in background regions (BGD). The hydrogen content measured for each sample is shown in horizontal rectangles.

The presence of OM influences the intensities in background regions (observable at high q values) (*e.g.* Anovitz & Cole, 2019) where background intensities (I_{BGD}) of intact samples are greater than those for combusted samples (Fig. 2). Additionally, in background regions, the intact-sample intensities are greater than the combusted-sample intensities (Fig. 1).

The hydrogen elemental determinations (Section S4) reveal that sample S1-NB presents a higher abundance (0.41%). Meanwhile, samples S51-NB and S52-NB yield lower abundances of 0.03 and 0.02%, respectively [Fig. 2(*c*)]. Thus, these data suggest a correlation between I_{BGD} and hydrogen abundance, as previously reported by Anovitz & Cole (2019).

### 3.2. Mineralogical degree of homogeneity and reliability of the two-phase system model

A homogenous mineralogical and chemical composition means that our samples can be reliably treated as two-phase silica–pore systems. Differences in X-ray SLD values and density of minerals need a spatial survey of mineralogic composition (Radlinski, 2006; Anovitz & Cole, 2015). Thus, we have used WAXS, Raman spectroscopy and μXRF to survey the mineralogical homogeneity of the samples.

Analysis of WAXS data yields a similar set of peaks regardless of the sample's age (Fig. 3). Specifically, a narrow variability in 2θ position is observed for peaks at 7.9, ~10.1, ~18.7 and ~24.8° (see the tables of Fig. 3). Using these positions, the software *QualX 2.0* identified alpha quartz predominantly occurring in the samples. For each peak, the absolute difference is less than 0.3% regarding 2θ positions of the quartz standard selected. Thus, this standard reproduces a goodness of fit better than 90%. A comparison between intact and combusted samples is included in Section S1.

The μXRF chemical maps show a strong predominance of silicon ubiquitously distributed across all samples, but other elements with high X-ray cross sections do not form visible grains in the maps (*e.g.* Fe). This latter fact could explain the homogenous X-ray transmission across the samples. In particular, Sr and Ca form micrometric sized grains of carbonate in sample S51. These mineral phases are sparsely distributed, with a proportion of less than 5% (see Section S2).

Similarly to WAXS in the intact samples, Raman microspectroscopy displays peaks typical for quartz, demonstrating the predominance of SiO$_2$ polymorphs (see Section S3). Peaks at 207 and 464 cm^{-1} indicate quartz occurrences in all samples. Additionally, peaks at 224, 422 and 501 cm^{-1} indicate the presence of cristobalite and moganite in sample S1 (Fig. S3.2 of the supporting information). Moganite and cristobalite have a water content (1.5–8%) higher than the abundances in quartz (<0.5%; Graetsch, 1994). The absence of moganite and cristobalite indicates dehydration in samples S52 and S51.

The WAXS, Raman and μXRF data prove the predominance of quartz in our cherts. Meanwhile, other less dense SiO$_2$ polymorphs, carbonate and possibly hematite, are minor phases composing the samples. This almost monomineralogic
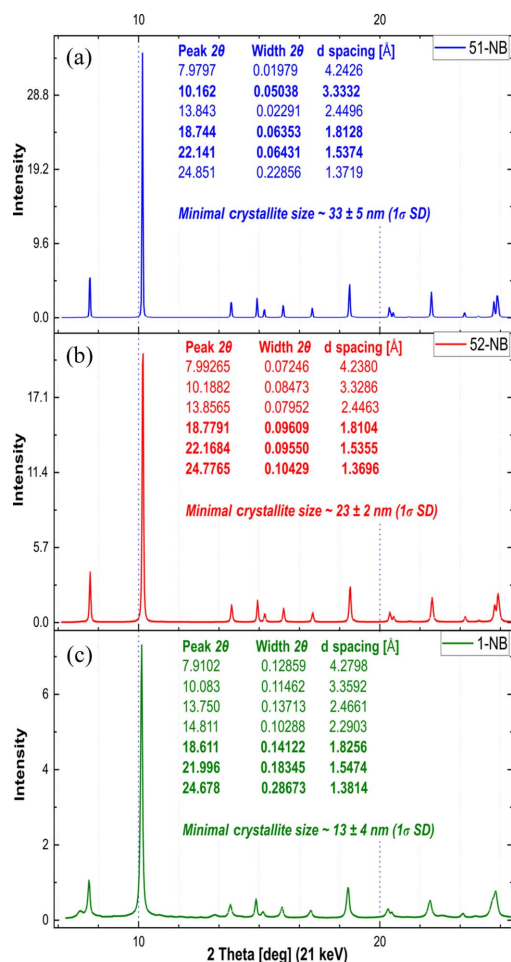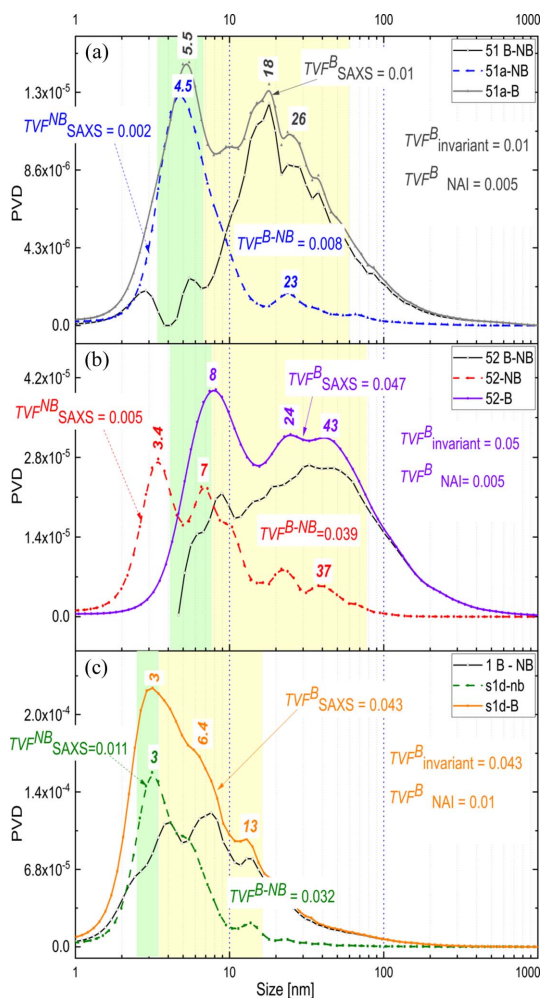
Figure 3
Peak diffraction profiles from intact samples (*a*) S51-NB, (*b*) S52-NB and (*c*) S1-NB. Tables in each diagram outline information for peaks identified using the WAXS fit tool in the *Irena* software. For each peak, the tables include center (2θ units), width (2θ units) and *d* spacing (ångström). Errors are less than 10% for each parameter. In each table, bold numbers highlight data used in crystallite-size calculation. These crystallite-size estimations are explained in Section S1.

composition consists of silica particles + pores, such as the two-phase source of scattering in combusted samples.

The OM presence could imply a third phase in intact samples. SLDs of OM estimated via equation (2) yield values from 0.22×10^{11} cm^{-2} (sample S1) to 1.53×10^{11} cm^{-2} (sample S51). These results are similar to SLDs of OM being less than half of the quartz SLD (Radlinski, 2006) and support that our intact samples behave as a quasi-two-phase system.

3.3. PVDs and pore-size hosting organics

The size distribution of pore volume is a primary factor controlling fluid mobilization into the pore matrix and provides microstructural information (Anovitz *et al.*, 2013). PVDs record the dissolution–precipitation process, which modifies porosity in sedimentary rocks (Lasaga, 1998; Emmanuel & Ague, 2009; Emmanuel *et al.*, 2010). PVDs exhibit multiple peaks (*i.e.* multimodal PVDs) and are non-uniform size distributions arising from pore-size-controlled

Figure 4
PVDs for intact and combusted samples [(*a*) sample S51, (*b*) sample S52 and (*c*) sample S1]. Segmented curves represent intact samples. Continuous curves represent combusted samples. Curves are colored according to the code used in previous figures. Difference PVD curves (ΔPVD) are shown in black. TVF$_{NAI}^B$ and TVF$_{invariant}^B$ represent the TVF of combusted samples estimated using N$_2$ adsorption isotherms and the invariant calculated via *Irena*, respectively. TVF^{B-NB} denotes the volume fraction released after combustion. Sizes in nanometres indicate scatterer-size peaks in the PVDs. TVF$_{SAXS}^B$ and TVF$_{SAXS}^{NB}$ represent the volume fractions calculated using SAXS analyses via the maximum entropy code in *Irena*. The pale-yellow regions denote scatterer sizes for which the scattering curves display power-law slopes between −3.2 and −3.5 for combusted samples. Pale-green areas represent Porod regions in combusted samples.

dissolution–precipitation processes (Emmanuel & Ague, 2009).

Semi-log diagrams show multimodal PVDs (Fig. 4). However, the PVD for sample S51-NB is practically one broad peak [blue curve, Fig. 4(*c*)]. Table 1 reports TVFs and other microstructural data.

The PVDs from the combusted samples are similar to the PVDs of the intact samples, suggesting the preservation of silica microstructure despite combustion (Fig. 4). Pores less than 500 nm in diameter represent the largest proportion of volume in all samples (Fig. 4). Meanwhile, micrometric pores are almost nonexistent.

Table 1
TVF and specific surface area for combusted and intact samples.

Numbers in parentheses represent uncertainty (1σ SD) in the last digits.

Combusted samples (silica matrix + pores).

Sample	Specific surface area ($m^2 g^{-1}$)		Pore volume (TVF)			
	Porod	BET	Invariant	MaxEnt	TNNLS	±
S51-B	0.88 (5)	0.5	0.011	0.009	0.012	0.006
S52-B	2.18 (16)	1.5	0.050	0.039 (1)	0.047 (1)	0.006
S1-B	11.5 (6)	3.0	0.043	0.041 (3)	0.042 (3)	0.106

Intact samples (silica matrix + OM + pores).

Sample	Specific surface area ($m^2 g^{-1}$)		Pore volume (TVF)			
	SSA	BET	Invariant	MaxEnt	TNNLS	NAI
S51-NB	0.63 (7)	0.25	0.002	0.002	0.003	0.003
S52-NB	1.12 (15)	0.30	0.005	0.005	0.006	0.004
S1-NB	9.3 (1)	21.4	0.012	0.011 (2)	0.013 (3)	0.022

Invariant: see Section 2.1.1. TNNLS: total non-negative least-squares method (see *Irena*'s manual; Ilavsky, 2021). NAI: TVF determined via N_2 adsorption–desorption isotherms (see Section S6). SSA: see Sections 2.1.2 and 3.6.

Table 1 reports TVF values calculated using the maximum entropy code (MaxEnt, TVF_{SAXS}^B and TVF_{SAXS}^{NB}) and the N_2 sorption method (BET, TVF_{BET}^B and TVF_{BET}^{NB}) (BET = Brunauer–Emmett–Teller theory). Generally, the $TVF_{SAXS}^{B,NB}$ values are greater than the TVFs estimated via other methods. Similar differences have been reported for sedimentary rocks (Anovitz & Cole, 2019).

The difference PVD curve defined as $\Delta PVD = PVD_{SAXS}^B - PVD_{SAXS}^{NB}$ (Fig. 4) quantifies the pore volume released by combustion. ΔPVD shows that a large fraction of the large pores were originally filled with OM [Figs. 4(b) and 4(c)]. Additionally, the ΔPVD curves indicate that a great proportion of the pores of less than 500 nm hosted organics.

The pore sizes hosting OM vary according to the geological age of the sample. The area below the ΔPVD curves supports this statement. In Fig. 4, such areas represent pores in Porod regions (pale green) and power-law slopes varying from −3.2 to −3.5 (pale yellow). Thus, pores in Porod regions host a minimal volume of OM, up to 2%, as indicated by the area below the ΔPVD curves in the pale-green region (Fig. 4).

In Fig. 4, the pale-yellow regions represent pores hosting from 37 to 60% of total OM. In these regions, the pores range from ∼4 to 20 nm for sample S1 and from ∼8 to 60 nm for the older samples (S51 and S52). In addition, pores in regions where the power-law slopes have a value of around −2.4 represent 30–50% of the total OM (white right-tail areas, Fig. 4). These pores range from 20 to 200 nm in sample S1 and from ∼100 to 500 nm for samples S51 and S52.

At this point, we can assume that (1) the PVDs from the combusted samples could be considered as a microstructural reference frame and that (2) pores less than 500 nm in diameter are filled with organics. Under these assumptions, the ΔPVD curves outline how OM is distributed into the pore network. Thus, the pores sized from ∼8 to 60 nm host up to 60% of OM in older samples. In contrast, the younger samples

host a smaller proportion (∼38%) in smaller pores (∼4 to 20 nm). Hence, OM is hosted by larger pores as the geological age of samples increases. This observation could point to the transport of OM from smaller to larger pores during burial and geological time. The transportation of OM occurring inside the porous matrix of sedimentary rocks was previously suggested by Anovitz & Cole (2015).

Pores in the Porod region accumulate a minimum of OM (up to 2%, Fig. 4). Moreover, pores in the Porod region are slightly larger in the older samples (∼4 to ∼8 nm) than in sample S1 (∼3 nm). Additionally, the ΔPVD curve is non-null beyond the Porod region down to the background in samples S1 and S51 [Figs. 4(a) and 4(b)]. This latter feature points to pores occurring in OM and supports similar interpretations in Section 3.1. Occurrences of such porosity have been reported (Anovitz & Cole, 2015).

3.4. Microstructural and geochemical data disclose geological processes experienced by chert samples

Chert samples of different ages were collected to monitor microstructural changes across geological timescales. The younger sample (sample S1) is a radiolarian chert collected from International Ocean Discovery Program (IODP) site 1149B (∼31.5°N) at 305 m below the sea floor at the magnetic anomaly M11 (∼132 Ma, late Valanginian age), Nadezhda Basin (Plank *et al.*, 2000).

Sample S1's location was selected because of the absence of both igneous intrusions and stratigraphic disturbances by faulting (Plank *et al.*, 2000). Both facts exclude hydrothermal alteration, igneous activity or metamorphism affecting the microstructure of chert. Instead, the data suggest that silica diagenesis is the unique geological process affecting the microstructure of sample S1.

Quartz, cristobalite–tridymite and carbonate were detected by Plank *et al.* (2000). Our μXRF maps rule out mineralogy sourced by hydrothermal processes in the S1 sample (Section S2). Along with quartz, our Raman microspectroscopy data show the presence of moganite, hematite and apatite, and the absence of carbonate (Section S3). The average pore volume in sample S1 (Table 1) is close to the porosity of ∼5% reported by Plank *et al.* (2000) for chert. A sedimentation rate of 20 m Ma^{-1} was suggested for Valanginian strata by Plank *et al.* (2000).

The older samples, S51 and S52, were collected from ancient continental tectonic blocks. Sample S52, with an estimated age of ∼1 Ga (Ga = billion years), was collected from the Narssârssuk Formation, Western Greenland (Strother *et al.*, 1983). Sample S51, collected from the Gunflint Formation at the northern border of Lake Superior, corresponds to a stromatolitic chert with an estimated age of ∼1.88 Ga (Barghoorn & Tyler, 1965; Fralick *et al.*, 2002).

Famous for its fossiliferous content, the Gunflint Formation is formed by a chemical-clastic succession of rocks with a U–Pb age of ∼1.88 Ga (Fralick *et al.*, 2002). There is no consensus about the predominant tectonic setting when Gunflint Formation rocks were deposited (Fralick *et al.*, 2002). Thus, in

the case of the Gunflint Formation, it could be highly speculative to assume specific values for tectonic parameters controlling diagenesis, such as thermal and pressure gradients, time of burial, and vertical movements of the crust (Siever, 1979).

On the basis of Raman data, Alleon *et al.* (2016) suggested that cherts from the Gunflint Formation have experienced a maximum temperature of 220°C, a typical temperature reported for diagenesis. Also, these authors reported silicon isotope signatures suggesting no hydrothermal quartz in Gunflint cherts. Our chemical and µXRF data (Section S2) rule out the presence of mineralogy formed by hydrothermal processes, which agrees with observations by Alleon *et al.* (2016).

Cherts from the Narssârssuk Formation (S52) contain well preserved microfossils interpreted as remnants of cyano-bacterial communities (Strother *et al.*, 1983). To the best of our knowledge, there is scarce information about the tectonic setting of the Narssârssuk Formation, which is mainly composed of limestones and other chemical sedimentary rocks deposited in an arid coastal environment (Strother *et al.*, 1983). Petrographic evidence indicates that cherts are diagenetic in origin (Strother *et al.*, 1983). Our petrographic data support this interpretation because hydrothermal or metamorphic minerals are absent. Also, Raman and µXRF data rule out the presence of mineralogy formed by hydrothermal processes (Sections S2 and S3).

Previous information about the tectonic settings is only crystal clear for the Cretaceous sample. This fact makes it difficult to interpret the influence of tectonic setting on diagenesis in older samples (S51 and S52). Instead, previous geochemical information and our data reinforce that diagenesis drives porosity evolution in time in our sample set.

3.5. WAXS and FESEM data: morphology evolution of silica particles

In this section, we survey the modifications in silica particles and how they could be related to changes revealed by (U)SAXS. The WAXS data in the tables of Fig. 3 indicate a systematic decrease in the FWHM of peaks. The Scherrer formula was used to calculate the minimal crystallite size in the intact and combusted samples. The details about these calculations are outlined in Section S1. In brief, we used a Scherrer constant of $K_{sh} \simeq 0.71$, $\lambda = 0.590401$ Å, integral breadth values and 2θ positions. Thus, we estimated a minimal crystallite size varying from 13 ± 4 nm (1σ SD) to 33 ± 5 nm (1σ SD) for samples S1-NB and S51-NB, respectively (Fig. 3). This increasing trend in crystallite sizes is to be expected because compaction by confining pressure has been operating over longer geological periods on silica microstructure.

Crystallite size after combustion is similar to the sizes calculated for the intact samples (Section S1 and Fig. S1). In addition, no peak typical of high-temperature SiO_2 polymorphs (tridymite) was observed on the WAXS profiles (Fig. S1). Both facts suggest a minimal effect from combustion on the sample microstructure.

The FESEM images show aggregates of silica particles distributed across the samples (Fig. 5). We have analyzed the change of particle shape at different magnifications using segmentation analysis, which revealed changes in the circularity of the particles. For example, sample S1 displays mostly circular silica particles, and clusters form greater and more prolate aggregates [Figs. 5(a) and 5(b)]. Sample S51 shows mostly elongated silica particles [Fig. 5(d)], while sample S52 exhibits smaller circular grains, which aggregate, forming more prolate particles [Fig. 5(c)] than sample S1.

FESEM-based particle-size histograms reveal similar size ranges for silica particles in all samples (Section S5). The
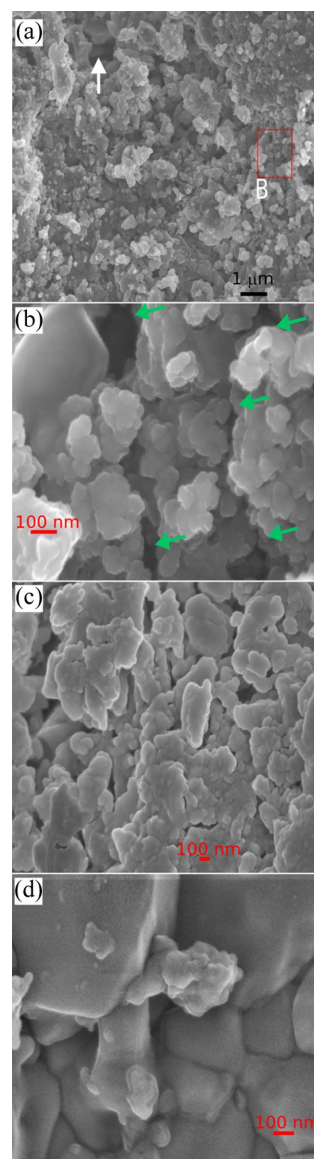
Figure 5
Secondary-electron FESEM images from samples (*a*), (*b*) S1, (*c*) S52 and (*d*) S51. Images were collected at magnifications of (*a*) 10 000×, (*b*) 100 000×, (*c*) 40 000× and (*d*) 80 000×. In (*a*), the white arrow highlights a rare micrometric pore. The red box denotes the position of magnification (*b*) in (*a*). In (*b*), green arrows display nanometric pores of irregular shape. In (*a*), the black bar denotes the scale. The red bars represent the scale in (*b*), (*c*) and (*d*).

minimal size varies from 25 to 30 nm, while the maximal sizes are around 450 nm. Images of lower magnification show the rare occurrence of some micrometric grains [Fig. 5(*a*)]. Sub-100 nm silica particles cover a greater proportion than particles over 100 nm in diameter (Section S5 and Fig. S5.1).
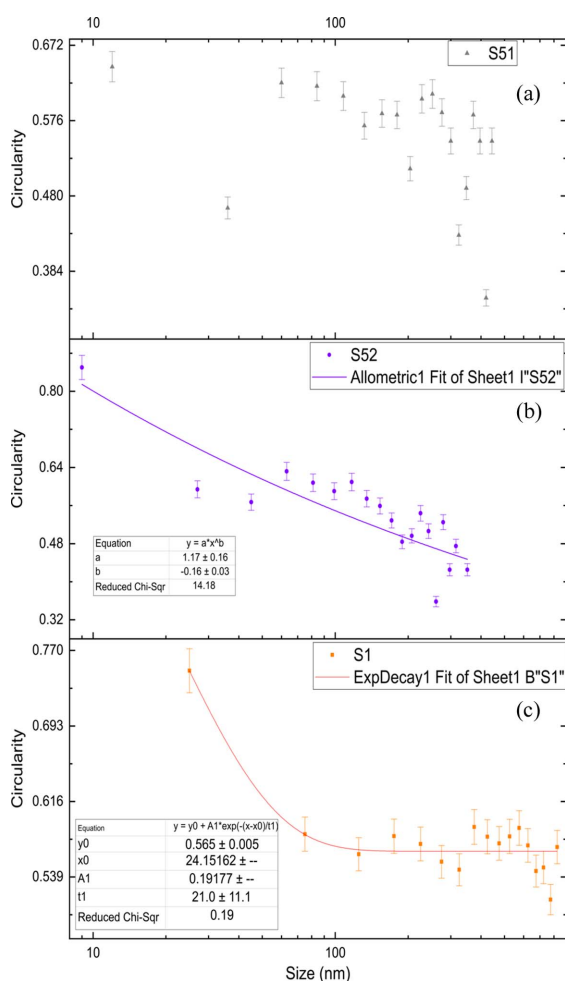
Our semi-log size versus circularity diagrams show decreasing trends (Fig. 6). Each diagram includes the statistical analysis of over 950 particles. Specifically, particles greater than 100 nm show lower circularity values. Meanwhile, sub-50 nm particles display circularity values above 0.65. Considering that circularity is inversely proportional to aspect ratio, we state that the greater the particle's size, the greater its aspect ratio. Details about Fig. 6 are provided in Section S5.

Congruently with the PVD data (Fig. 4), the secondary-electron images of the combusted samples (Section S5 and Fig. S5.3) show greater porosity than those of the intact samples (Fig. 5). Despite the high temperature attained in the combustion of samples (~1000°C, Section S8), the particles

Figure 6
Circularity versus the size of silica particles. Data from analysis of FESEM images. Continuous curves represent the fit for each sample. Diagram (*a*) shows a rough decreasing trend, which it is difficult to fit using an exponential model [*e.g.* in (*c*) for sample S1] or a power-law model [see (*b*) for sample S52]. Overall, errors in circularity (1σ SD) are less than 3%; see more details in Section S5. In (*b*) and (*c*), bins for sizes larger than 500 nm were discarded since they concentrated a scarce quantity of particles.

were not significantly affected by combustion. Specifically, the shape and size of the particles were not significantly affected (see Fig. S5.3 versus Fig. 5).

Combusted samples were exposed for less than 5 min to 1000°C. Thus, changes by annealing could be minimized because quartz-melting experiments have shown melting effects on quartz after combustion up to 1700°C for 10 min or 1570°C for 200 min (Ainslie *et al.*, 1961). But our WAXS data are not conclusive enough to rule out nanoscale diffusion effects. Thus, we plan to perform electron backscatter diffraction experiments to gain further insight into crypto diffusion effects or the presence of tridymite nanocrystals (quartz–tridymite transition occurs at 870°C).

Changes in silica particle morphology influence the pore shape. For example, Figs. 5(*c*) and 5(*d*) show slit-like pores, which are expected given the predominance of more elongated silica particles. Additional N_2 sorption data support slit-like pores in the older samples (S51-B and S52-B) (Section S6). The predominance of more circular silica particles determines more isometric pores in sample S1 [Figs. 5(*a*) and 5(*b*)].

3.6. Microstructural evolution and associated changes in volatile contents

The mineralogical changes outlined above are indicative of chemical changes occurring from younger to older samples. Raman data indicate the presence of moganite and cristobalite in sample S1. Also, Raman data support the absence of these hydrated silica polymorphs in the older samples (S52 and S51). Hence, progressive dehydration possibly predominates in older samples. This hypothesis led us to analyze the chemical data collected in our samples.

In our rocks, volatile compounds were quantified using CHN elemental analysis (Section S4), GC–MS (Section S7) and TGA (Section S8). The TGA outputs show that the abundance of volatile compounds decreases as geological age increases. This is an expected trend as compaction induces the dehydration of unconsolidated sedimentary deposits (*e.g.* Williams *et al.*, 1985).

In older samples, the carbon abundances correspond to a significant proportion of the total volatile contents (Tables S4 and S7 of the supporting information). Carbon abundances vary from 0.7% (S52) to 0.17% (S51). Meanwhile, total volatile values of 0.87 and 0.26% were measured for samples S52 and S51, respectively. This suggests that organic molecules are the source of the carbon in the samples.

Table S4 shows that carbon is less abundant than hydrogen in the younger sample (sample S1). Meanwhile, carbon is more abundant than hydrogen in the older samples. These data point to a carbon enrichment in older samples.

Table S4 compares CHN total abundance versus volatile abundances estimated from the second stage of the TGA curves. In samples S51 and S52, CHN abundances are equal to volatile abundances quantified by TGA. In addition to carbon, hydrogen and nitrogen are still bonded to organic molecules in our samples.

The hydrogen abundances decrease from 0.4% (sample S1) to 0.03% (samples S51 and S52, Table S4). Another source of hydrogen could be hydroxyl functional groups such as silanol groups (Si—OH) on the quartz surface. This decrease points to progressive dehydration of the older samples (S51 and S52). Dehydration of confined sediments is a common observation in studies dealing with siliceous rock formation (*e.g.* Williams *et al.*, 1985; Chaika & Williams, 2001; Wrona *et al.*, 2017).

SAXS and chemical data support a reduction in pore volume associated with the progressive dehydration of silica deposits. This phenomenon explains the low volatile contents of 0.87 and 0.26% observed in samples S52 and S51, respectively (versus 3.64% in sample S1). Compaction under confinement is the primary factor inducing a reduction in pore volume.

In addition, the formation of sedimentary rocks includes dissolution–precipitation reactions. Such reactions can be understood via the pore-size-controlled solubility model (PCS; Emmanuel & Ague, 2009) and the constant solubility model (Lasaga, 1998). In the PCS model, solubility exhibits a non-linear dependence on the size of crystals and pores (r), interfacial free energy (γ), temperature (T), and molar volume of the minerals (Emmanuel & Ague, 2009). Thus, increasing γ or decreasing r induces an enhancement of the crystal's solubility. Hence, permeability reduction occurs given the pore throat closes, isolating the smaller pores from exogenous fluids and locally precluding the mobility of OM (Stack, 2015).

For example, the PCS model predicts silica dissolution in sandstone pores smaller than 8 μm (Emmanuel *et al.*, 2010). But γ varies strongly according to the liquid phase in contact with silica particle surfaces (Parks, 1984; Dove *et al.*, 2008). This variation in γ could support silica dissolution mostly in pores less than 100 nm and permit OM preservation.

3.7. Initial insights into OM preservation in silica-rich sedimentary rocks and future directions

The evolution of mechanisms incorporating volatile species into mineral-porous matrices could influence the OM preservation inside chert. For example, van der Waals and hydrogen-bonding interactions mediate water incorporation in minerals (Eckert *et al.*, 2015). Beyond this, modification in interactions between organics and minerals possibly occurs in response to a time evolution experienced by the silica particle-porous matrix. Thus, to obtain initial insights into these interactions, we must address issues such as pore size, variation of the SSA over geological time, organic molecule sizes and SLDs for OM deduced from SAXS curves.

SAXS experiments provide critical evidence supporting possibly electrostatic driven interactions among silica nano-particles and organics (*e.g.* van den Heuvel *et al.*, 2018). The sizes of pores holding OM raise this hypothesis. For instance, electrostatic interactions are long range and significant below 100 nm sizes (Israelachvili, 2011). Specifically, our PVD data possibly support the interaction between silica particles and organic aromatic clusters in pores of less than 500 nm.

Moreover, the most significant volume fraction of organics is held in pores of less than 100 nm in diameter.

Silica is negatively charged over a wide range of pH values (Williams & Crerar, 1985). Meanwhile, several organic molecules are positively charged (*e.g.* van den Heuvel *et al.*, 2018). Consequently, long-range interactions between OM and silica could be attractive in a cation-bearing aqueous solvent.

At nanometre sizes, some intrinsic properties scale with the SSA, becoming additive in nature (surface-area-to-volume effects; Israelachvili, 2011). This inherent property refers to the adhesion energy among silica particle surfaces and organic aromatic clusters. Thus, this energy, combined with hydrophobic organics hosted in locally isolated pores, could explain the OM preservation into chert. The adhesion energy is directly proportional to the interfacial free energy of the surface. This energy is also inversely proportional to the elastic modulus (Israelachvili, 2011). Thus, the lower the elastic modulus, the higher the adhesion energy (Israelachvili, 2011).

The interfacial free energy is proportionally inverse to the variation in the area of a surface [$\gamma = (\partial G/\partial A)_{P,T,n}$; Adamson, 1982; Parks, 1984]. Hence, quantifying SSA could provide initial insights into this adhesion. SSA is a key physical quantity influencing mineral precipitation, dissolution rates, reactive-transport equations and reaction kinetics (Emmanuel & Ague, 2009). In our case, this quantity could be decisive in understanding the adhesion of organics to the silica interface.

For the combusted samples, the analysis of SAXS data from the Porod region yielded a decreasing SSA as the geological ages of the samples increased. Specifically, SSA decreases from 11.5 to 0.88 m^2 g^{-1} for S1-B and S51-B, respectively, with S52-B yielding an intermediate SSA value of 2.18 ± 0.16 m^2 g^{-1}. Similarly for intact fragments, the SSA values decrease from younger to older samples.

The SSA values for the combusted samples are greater than those yielded for the intact samples (Table 1). For example, the SSA varies from 11.5 ± 0.6 m^2 g^{-1} (S1-B) to 9.28 ± 1.41 m^2 g^{-1} (S1-NB). Samples S51 and S52 displayed similar variation. To understand this trend, we adapted equation (4):

$$\left(\frac{S}{V}\right)_r^B = \left(\frac{S}{V}\right)_0^B \left(\frac{r}{r_0}\right)_B^{-\alpha_B - 4} \tag{5a}$$

and

$$\left(\frac{S}{V}\right)_r^{NB} = \left(\frac{S}{V}\right)_0^{NB} \left(\frac{r}{r_0}\right)_{NB}^{-\alpha_{NB} - 4}. \tag{5b}$$

The microstructure could be considered a reference frame (Section 3.3). Thus, $(S/V)_0^{NB} \simeq (S/V)_0^B$ and $r_0^{NB} \simeq r_0^B$. Additionally, pore-size peaks in PVD diagrams are similar in both combusted and intact samples, so $r_B \simeq r_{NB} \cong r$. Under these simplifications, dividing equation (5b) by (5a) yields

$$\frac{(S/V)_r^{NB}}{(S/V)_r^B} = \frac{SSA_r^{NB}}{SSA_r^B} \simeq r^{\alpha_B - \alpha_{NB}}. \tag{6}$$

Considering the average power-slope values for pore-size ranges in the pale-yellow areas in Figs. 4 and 5, we obtain negative ($\alpha_B - \alpha_{NB}$) values varying from −0.45 (sample S52)

to −0.24 (sample S1). Thus, the modified version of Allen's model explains the SSA variation induced by combustion given that $SSA_r^{NB} < SSA_r^B$. This stems from the combustion release of OM adsorbed on silica's particle surfaces.

This extension of Allen's model permits one to gain insights into the influence of OM on the S/V ratio. To address this influence, we calculated ratios between SSAs from the intact samples. Table 1 reports the calculated SSA values for the intact samples using this extension. For example, the $SSA_{S52}^{NB}/SSA_{S51}^{NB}$ ratio yields a value of ~1.8 ± 0.3 (1 σ SD). Additionally, for the $SSA_{S1}^{NB}/SSA_{S51}^{NB}$ ratio, we obtain a value of 15.3 ± 0.1 (1 σ SD).

Allen's model reveals a decreasing SSA from sample S1-NB to the older intact samples (S52-NB and S51-NB). The BET method also shows a similar SSA decreasing trend (Table 1). Congruently, OM abundances decrease from younger to older samples (see Sections S4 and S7). In conjunction with these chemical data, the application of this model suggests that the lower the OM abundance, the lower the SSA covered by OM. This is an expected effect of OM adhesion, as suggested by the Gibbs adsorption equation (Israelachvili, 2011).

The size of organic molecules provides critical information about their preservation in a mineral-porous matrix. Simultaneously, Raman microspectroscopy allows estimating the size of a cluster of carbonaceous OM. That is, organic molecules yield a spectral response that exhibits bands typical for graphite (D and G bands located at 1350 and 1580 cm^{-1}; Foucher, 2019).

Raman data from our samples (see Section S3) show distinct spectra according to geological age. The representative Raman spectrum for sample S1 displays six broad peaks in the region from 1000 to 2000 cm^{-1} (see Section S3, Fig. S3.2). This spectral region exhibits spectral bands of several organic molecules that do not match with both D and G bands. Hence, this fact permits us to rule out graphite occurrence in sample S1. Conversely, the older samples show graphitic bands (see Section S3, Fig. S3.1).

The FWHM values for the D and G peaks in sample S51 are less than those of S52, indicating a more significant carbonization progression in the older sample (S51) (Fig. S3.1). Additionally, the intensities of the D and G bands yield a similar size of 20 ± 1.0 nm for polyaromatic carbon units for both S51 and S52. Appendix A2 provides details about the calculation of these aromatic cluster sizes.

Alternatively, the hydrogen/carbon (H/C) ratio permits estimating the sizes of organics occurring in an OM-bearing rock. This fact arises from polyaromatic carbons forming domains of greater size as temperature and time increase (Ferralis *et al.*, 2016). These authors reported a correlation between the H/C ratio and the size of a round aromatic cluster. Thus, using H/C $\simeq$ 0.17 from sample S51, we estimated aromatic clusters ranging from 2 to 4 nm in the older samples. In conjunction, our data reveal polyaromatic carbon clusters ranging from 2 to 20 nm in size. Therefore, pores ranging from 8 to 56 nm could preferentially host these aromatic clusters [Figs. 4(*b*) and 4(*c*)]. These pore sizes contain a more significant proportion of OM.

As reported in Section 3.2, application of equation (2) yielded SLDs of OM from 0.22 × 10^{11} cm^{-2} (sample S1) to 1.53 × 10^{11} cm^{-2} (sample S51). These SLDs of OM (SLD-OM) yielded a decreasing contrast for the intact samples varying from 4.1 × 10^{22} cm^{-4} (in S1-NB) to 5.1 × 10^{21} cm^{-4} (in S51-NB). The intact sample S1-NB possessed the greater contrast value [$|\Delta\rho|_{NB}^2 = (\rho_{sil} - \rho_{OM})^2$], inducing greater scattering intensities than observed for the older samples [Figs. 2(*b*) and 2(*c*)].

Our SLD-OM results agree with the SLD values reported by Radlinski (2006). Furthermore, our results outline an increasing SLD-OM trend from younger (S1-NB) to older samples (S52-NB and S51-NB). This trend is possibly associated with differences in OM. Carbonaceous and kerogen-rich OM yields higher SLDs (~1.3 × 10^{11} cm^{-2}; Radlinski, 2006). Meanwhile, the same authors report an SLD ranging from ~0.5 × 10^{11} to ~1 × 10^{11} cm^{-2} for hydrogen-bearing OM. In this regard, our SLD-OM results agree with Raman, CHN abundances and previous SLD-OM data to show OM evolution over geological time. The OM evolved from hydrogen rich to carbonaceous-kerogen rich in our rocks.

A final consideration arises from PVDs. Ostwald ripening of crystals can generate a monodispersed and uniformly distributed pore-size population (Mehmani & Xu, 2022). Alternatively, bimodal PVDs have been interpreted as the result of mineral precipitation and dissolution controlled by pore size (PCS; Emmanuel & Ague, 2009). Our PVDs exhibit up to four peaks (Fig. 4), possibly supporting PCS as a mechanism that operated in our rocks. Thus, silica dissolution could be favored in nanometric pores. Pores smaller than 60 nm holding a higher proportion of organics (Fig. 4) support this hypothesis because silica dissolution would have occurred inside these sub-100 nm pores. Together with SSA trends, this final consideration advocates documenting the interfacial free energy variation in our samples.

4. Conclusions

Cherts of different geological ages were characterized by focusing on the microstructure and mineralogy of their inorganic component. These samples show an evolving silica-rich microstructure over geological timescales. The samples are homogeneously composed of alpha quartz as a predominant mineral phase. This mineral phase displays narrower diffraction peaks and shows increasing crystallite sizes up to 33 ± 5 nm (1σ SD) in the older chert samples. Secondary-electron images show silica particle shapes evolving from younger to older chert samples. Additionally, low water abundances in the older samples (~0.03%) suggest progressive dehydration.

(U)SAXS data reveal a porous matrix that evolves across geological time. This evolution includes the following changes from younger to older samples: (1) a decreasing pore volume down to 1%, (2) greater pore sizes hosting OM, (3) decreasing SSA values and (4) a lower background intensity correlated to decreasing hydrogen abundances.

Pores ranging from 4 to 100 nm accumulate the greater volume fraction of OM. Additionally, Raman data support

aromatic organic clusters up to 20 nm in the older samples. Thus, Raman data and PVDs support OM mostly in mesopores.

SAXS data yield a decreasing SSA from younger (9.3 ± 0.1 m^2 g^{-1}) to older intact samples (0.63 ± 0.07 m^2 g^{-1}, 1σ SD). The BET method also shows a similar SSA decreasing trend. Congruently, OM abundances decrease from younger to older samples. Thus, OM abundances and SSA trends suggest that the lower the OM abundance, the lower the SSA covered by OM.

Our data support that compaction under confinement modified the silica particle + organics + pore network over geological timescales. Compaction led to progressive dehydration, crystallization of more stable SiO$_2$ polymorphs and redistribution of OM inside pore networks. This porosity reduction possibly modifies how silica incorporates volatile compounds into its porous matrices. Thus, silica-organic interactions combined with hydrophobic organics could explain the OM preservation in chert. Finally, we are currently performing contact angle experiments to monitor the variation in interfacial free energy in our samples.

5. Related literature

The following references are cited in the supporting information for this article: Anovitz & Cole (2015), Drits (1997), Jacquat *et al.* (2011), Lele & Anantharaman (1966), Patterson (1939), Vargas *et al.* (1983) and Whiteside & Grice (2016).

APPENDIX *A*
Experimental details of chemical-sensitive and spectroscopy techniques

A1. X-ray microfluorescence mapping

X-ray fluorescence data were collected on the same intact fragments and regions studied via (U)SAXS. Experiments were performed at the 13-ID-E beamline (Advanced Photon Source) using an incident-beam energy of 17 keV. This energy permitted the detection of elements from strontium down to the silicon *K*α peak (at 1.839 keV). Elemental maps were scanned at 2 μm resolution. The maps were 800 by 600 μm (sample S1) and 1600 by 800 μm (sample S52) in area. A dwell time of 15 ms per pixel determined a total scan time of ∼2 h. The maps and XRF spectra were analyzed using the *Larch* tool (Newville, 2013).

A2. Raman microspectroscopy

Raman measurements were performed at IFSC-USP and IPEN-CNEN. On the same samples (intact and combusted) characterized at APS, Raman data were collected using Horiba LabRAM HR Evolution instruments. The instrumental setups were as follows: a laser of 785 nm, an objective of 50×, an acquisition time of some seconds, power between 1 and 100 mW, and a beam diameter ranging from ∼1.3 to 3 μm. Data were also collected using a laser of 532 nm on ancient chert samples. Processing included baseline subtraction and

smoothing. Post-processing mineral identification was performed using the RRUFF database (Lafuente *et al.*, 2015).

The spectral region between 1000 and 2000 cm^{-1} exhibits spectral bands for several organic molecules and carbonaceous matter (Foucher, 2019). This fact turns this region into one of high analysis interest.

For intact samples S52 and S51, we calculated the size of aromatic carbonaceous clusters using a modification of Tuinstra–Koenig formula (Mallet-Ladeira *et al.*, 2014):

$$L = \frac{4.4}{I_D/I_G}\left(\frac{2.41}{E_L}\right)^4,$$

where *L* represents the size of the aromatic cluster (in nanometres). The heights of the *D* and *G* bands (I_D, I_G) were calculated via deconvolution using *Origin*. E_L stands for incident-radiation energy (∼eV).

A3. CHN elemental determinations

Carbon, hydrogen and nitrogen were determined in a Perkin Elmer 2400 Elemental Analyzer equipped with a thermal conductivity detector (Chemistry Institute, USP). Sample powders (some milligrams) were combusted under an oxygen atmosphere.

A4. GC–MS and GC–FID

Quantitative determinations of aliphatic and polycyclic aromatic hydrocarbons (PAHs) were performed at IOUSP using an Agilent GC equipped with a flame ionization detector (GC–FID) and an Agilent GC coupled with a mass spectrometer (GC–MS). Organics were extracted from rock powders using a mixture of dichloromethane and *n*-hexane. Quantitation of organics was performed via an internal standard method. Lourenço *et al.* (2013) detail experimental procedures for aliphatic polycyclic aromatic hydrocarbon quantification.

APPENDIX *B*
Thermogravimetric analysis and N$_2$ physical sorption method

B1. Thermogravimetric analysis

Differential scanning calorimetry (DSC) and TGA measurements were performed using a simultaneous thermal analyzer (DSC/TGA), the Discovery SDT 650 from TA Instruments (UNIFESP). DSC/TGA curves were obtained at a heating rate of 10°C min^{-1} in a temperature range from room temperature to 1000°C, under dynamic air (100 ml min^{-1}) using a platinum crucible (110 ml).

B2. N$_2$ physical sorption method

Adsorption isotherms were obtained on a Micromeritics ASAP 2020 volumetric adsorption analyzer using nitrogen of 99.998% purity (IFUSP). Measurements were performed in a range of relative pressure from 10^{-6} to 0.99 (liquid nitrogen) on samples degassed at 200°C for 2 h. The SSA was estimated using the BET method (Brunauer *et al.*, 1938). The total pore

volume was calculated from the amount adsorbed at the relative pressure of 0.99. The pore-size distribution was calculated using the BJH algorithm (Barrett *et al.*, 1951).

APPENDIX *C*
Field-emission scanning electron microscopy

Intact fragments distinct from those measured by (U)SAXS were prepared for FESEM experiments performed with a JEOL JSM-7401F instrument at the Chemistry Institute (USP). We imaged samples via a high-resolution secondary-electron imaging detector (in-lens detector).

The preparation of surfaces was a critical step in our research (Section S5, Fig. S5.2). We employed three treatment procedures: (*a*) no treatment, exposing a fresh broken surface to the scanning electron microscope; (*b*) slicing and manual polishing of surfaces; and (*c*) HF-vapor (HF = hydrofluoric acid) etching of surfaces and subsequent manual polishing (1 h of etching). This last procedure yielded the best output, exposing the real microstructure of the chert (see Section S5). In addition, procedure (*a*) partially unveiled aggregates of the silica particles.

After etching, samples were coated using a 3–5 nm gold layer. Secondary-electron images were collected in vacuum mode using a potential between 3 and 5 keV and a work distance of 3 mm.

Secondary-electron images were obtained using magnifications varying from $250\times$ to $150\,000\times$. The images with magnifications from $40\,000\times$ to $120\,000\times$ yielded a nominal pixel edge length of $\sim$2.3 and 0.78 nm, respectively. FESEM instruments provide a best spatial resolution size of $\sim$5 nm (Anovitz & Cole, 2015). Thus, the smallest particles in the raw secondary-electron images are possibly $\sim$20 nm in diameter.

We processed the secondary-electron images using the *ImageJ* software (Abramoff *et al.*, 2004; Rasband, 1997–2016). Processing followed these steps: (1) scaling, (2) tophat filter using a minimal size of five pixels, (3) autothresholding to convert images to binary, (4) segmentation using the watershed algorithm and (5) measurement of parameters from binary images. Parameters quantified for *ImageJ* include area, perimeter, Feret's diameter, circularity and aspect ratio. In addition, *ImageJ* calculates the SDs about the average of each parameter. *ImageJ*-based segmentation identified at least 300 particles per image.

Data from *Image J* for three secondary-electron images per sample ($40\,000\times$) were used to calculate 1D histograms for particle size (*i.e.* Feret's diameter) and 2D histograms for particle size versus circularity via *Origin*. Overall, for particle size we selected a 12 nm-sized bin, and an automatic sized bin was used for statistics on circularity. Each histogram (Fig. S5.1) and size versus circularity curve (Fig. 6) used at least 950 particles.

Section S5 provides information about the particle-size distribution histograms (PSDs, Fig. S5.1). From these PSDs, we extracted data about circularity and silica particle diameter, which were plotted in Fig. 6.

Combusted fragments previously measured by (U)SAXS were used for FESEM in the JEOL JSM-7401F instrument at the Chemistry Institute (USP, June 2023). High-resolution secondary-electron images were collected (Section S5, Fig. S5.3) via a similar analytical setup to that used on the intact fragments.

References

Abramoff, M. D., Magalhães, P. J. & Ram, S. J. (2004). *Biophoton. Int.* **11**, 36–42.

Adamson, A. W. (1982). *Physical Chemistry of Surfaces*, 4th ed. New York: Wiley.

Ainslie, N. G., Mackenzie, J. D. & Turnbull, D. (1961). *J. Phys. Chem.* **65**, 1718–1724.

Allen, A. J. (1991). *J. Appl. Cryst.* **24**, 624–634.

Alleon, J., Bernard, S., Le Guillou, C., Marin-Carbonne, J., Pont, S., Beyssac, O., McKeegan, K. D. & Robert, F. (2016). *Nat. Commun.* **7**, 11977.

Alleon, J. & Summons, R. E. (2019). *Free Radical Biol. Med.* **140**, 103–112.

Altomare, A., Corriero, N., Cuocci, C., Falcicchio, A., Moliterni, A. & Rizzi, R. (2015). *J. Appl. Cryst.* **48**, 598–603.

Anovitz, L. M. & Cole, D. R. (2015). *Rev. Mineral. Geochem.* **80**, 61–164.

Anovitz, L. M. & Cole, D. R. (2019). *Geological Carbon Storage*, Geophysical Monograph Series, Vol. 238. Washington, DC: American Geophysical Union.

Anovitz, L. M., Cole, D. R., Rother, G., Allard, L. F., Jackson, A. J. & Littrell, K. (2013). *Geochim. Cosmochim. Acta*, **102**, 280–305.

Armstrong-Altrin, J. S. & Verma, S. P. (2005). *Sediment. Geol.* **177**, 115–129.

Bahadur, J., Melnichenko, Y. B., Mastalerz, M., Furmann, A. & Clarkson, C. R. (2014). *Energy Fuels*, **28**, 6336–6344.

Barghoorn, E. S. & Tyler, S. A. (1965). *Science*, **147**, 563–575.

Barrett, E. P., Joyner, L. G. & Halenda, P. H. (1951). *J. Am. Chem. Soc.* **73**, 373–380.

Brunauer, S., Emmett, P. H. & Teller, E. (1938). *J. Am. Chem. Soc.* **60**, 309–319.

Chaika, C. & Williams, L. A. (2001). *Am. Assoc. Pet. Geol. Bull.* **85**, 149–167.

Chester, J. S., Lenz, S. C., Chester, F. M. & Lang, R. A. (2004). *Earth Planet. Sci. Lett.* **220**, 435–451.

Dove, P. M., Han, N., Wallace, A. F. & De Yoreo, J. J. (2008). *Proc. Natl Acad. Sci. USA*, **105**, 9903–9908.

Drits, V. (1997). *Clays Clay Miner.* **45**, 461–475.

Eckert, J., Gourdon, O., Jacob, D. E., Meral, C., Monteiro, P. J. M., Vogel, S. C., Wirth, R. & Wenk, H.-R. (2015). *Eur. J. Mineral.* **27**, 203–213.

Emmanuel, S. & Ague, J. J. (2009). *Water Resour. Res.* **45**, W04406.

Emmanuel, S., Ague, J. J. & Walderhaug, O. (2010). *Geochim. Cosmochim. Acta*, **74**, 3539–3552.

Ferralis, N., Matys, E. D., Knoll, A. H., Hallmann, C. & Summons, R. E. (2016). *Carbon*, **108**, 440–449.

Foucher, F. (2019). *Biosignatures for Astrobiology*, edited by B. Cavalazzi & F. Westall. Heidelberg: Springer Nature.

Fralick, P., Davis, D. W. & Kissin, S. A. (2002). *Can. J. Earth Sci.* **39**, 1085–1091.

Graetsch, H. (1994). *Rev. Mineral. Geochem.* **29**, 209–232.

Graetsch, H. & Ibel, K. (1997). *Phys. Chem. Miner.* **24**, 102–108.

Gražulis, S., Chateigner, D., Downs, R. T., Yokochi, A. F. T., Quirós, M., Lutterotti, L., Manakova, E., Butkus, J., Moeck, P. & Le Bail, A. (2009). *J. Appl. Cryst.* **42**, 726–729.

Gražulis, S., Daškevič, A., Merkys, A., Chateigner, D., Lutterotti, L., Quirós, M., Serebryanaya, N. R., Moeck, P., Downs, R. T. & Le Bail, A. (2012). *Nucleic Acids Res.* **40**, D420–D427.

Heuvel, D. B. van den, Stawski, T. M., Tobler, D. J., Wirth, R., Peacock, C. L. & Benning, L. G. (2018). *Front. Mater.* **5**, 19.

Hinman, N. W. (1990). *Geochim. Cosmochim. Acta*, **54**, 1563–1574.

Ilavsky, J. (2012). *J. Appl. Cryst.* **45**, 324–328.

Ilavsky, J. (2021). *Irena and Nika Documentation*, https://saxs-igorcodedocs.readthedocs.io/en/stable/.

Ilavsky, J. & Jemian, P. R. (2009). *J. Appl. Cryst.* **42**, 347–353.

Ilavsky, J., Jemian, P. R., Allen, A. J., Zhang, F., Levine, L. E. & Long, G. G. (2009). *J. Appl. Cryst.* **42**, 469–479.

Ilavsky, J., Zhang, F., Allen, A. J., Levine, L. E., Jemian, P. R. & Long, G. G. (2013). *Metall. Mater. Trans. A*, **44**, 68–76.

Israelachvili, J. N. (2011). *Intermolecular and Surface Forces*, 3rd ed. Amsterdam: Elsevier.

Jacquat, O., Rambeau, C., Voegelin, A., Efimenko, N., Villard, A., Föllmi, K. B. & Kretzschmar, R. (2011). *Swiss J. Geosci.* **104**, 409–424.

Kotzias, D., Herrmann, M., Zsolnay, A., Beyerle-Pfnür, R., Parlar, H. & Korte, F. (1987). *Chemosphere*, **16**, 1463–1468.

Lafuente, B., Downs, R. T., Yang, H. & Stone, N. (2015). *Highlights in Mineralogical Crystallography*, edited by T. Armbruster & R. M. Danisi, pp. 11–30. Berlin: De Gruyter.

Lasaga, A. C. (1998). *Kinetic Theory in the Earth Sciences.* New Jersey: Princeton University Press.

Lele, S. & Anantharaman, T. R. (1966). *Proc. Indian Acad. Sci.* **64**, 261–274.

Lourenço, R. A., Araujo Júnior, M. A. G., Meireles Júnior, R. O., Macena, L. F., de, A., Lima, E. F. & Carneiro, M. E. R. (2013). *Continental Shelf Res.* **71**, 37–44.

Mallet-Ladeira, P., Puech, P., Toulouse, C., Cazayous, M., Ratel-Ramond, N., Weisbecker, P., Vignoles, G. L. & Monthioux, M. (2014). *Carbon*, **80**, 629–639.

Marks, B., Sandnes, B., Dumazer, G., Eriksen, J. A. & Måløy, K. J. (2015). *Front. Phys.* **3**, 41.

McCarthy, J. F., Ilavsky, J., Jastrow, J. D., Mayer, L. M., Perfect, E. & Zhuang, J. (2008). *Geochim. Cosmochim. Acta*, **72**, 4725–4744.

Mehmani, Y. & Xu, K. (2022). *J. Comput. Phys.* **457**, 111041.

Moreau, J. W. & Sharp, T. G. (2004). *Astrobiology*, **4**, 196–210.

Natalio, F., Corrales, T. P., Pierantoni, M., Rosenhek-Goldian, I., Cernescu, A., Raguin, E., Maria, R. & Cohen, S. R. (2021). *Chem. Geol.* **582**, 120427.

Newville, M. (2013). *J. Phys. Conf. Ser.* **430**, 012007.

Parks, G. A. (1984). *J. Geophys. Res.* **89**, 3997–4008.

Patterson, A. L. (1939). *Phys. Rev.* **56**, 978–982.

Plank, T., Ludden, J. N., Escutia, C. *et al.* (2000). *Proc. ODP Init. Repts*, **185**, http://www.iodp.tamu.edu/publications/185_IR/185IR.PDF.

Radlinski, A. (2006). *Rev. Mineral. Geochem.* **63**, 363–397.

Radlinski, A., Ioannidis, M., Hinde, A., Hainbuchner, M., Baron, M., Rauch, H. & Kline, S. (2004). *J. Colloid Interface Sci.* **274**, 607–612.

Rasband, W. S. (1997–2016). *ImageJ*, US National Institutes of Health, Bethesda, Maryland, USA, https://imagej.nih.gov/ij/.

Scherer, M. (1987). *Am. Assoc. Pet. Geol. Bull.* **71**, 485–491.

Siever, R. (1979). *J. Geol.* **87**, 127–155.

Stack, A. (2015). *Rev. Mineral. Geochem.* **80**, 165–190.

Stein, C. L. & Kirkpatrick, R. J. (1976). *J. Sed. Res.* **46**, 430–435.

Strother, P. K., Knoll, A. H. & Barghoorn, E. S. (1983). *Paleontology*, **26**, 1–32.

Taylor, T. T., Giles, M. R., Hathon, L. A., Diggs, T. N., Braunsdorf, N. R., Birbiglia, G. V., Kittrigde, M. G., Macaulay, C. I. & Espejo, I. S. (2010). *Am. Assoc. Pet. Geol. Bull.* **94**, 1093–1132.

Thomas, J. J., Jennings, H. M. & Allen, A. J. (1998). *Cem. Concr. Res.* **28**, 897–905.

Vargas, R., Louër, D. & Langford, J. I. (1983). *J. Appl. Cryst.* **16**, 512–518.

Wacey, D., McLoughlin, N., Kilburn, M. R., Saunders, M., Cliff, J. B., Kong, C., Barley, M. E. & Brasier, M. D. (2013). *Proc. Natl Acad. Sci. USA*, **110**, 8020–8024.

Whiteside, J. H. & Grice, K. (2016). *Annu. Rev. Earth Planet. Sci.* **44**, 581–612.

Williams, L. A. & Crerar, D. A. (1985). *J. Sediment. Petrol.* **55**, 312–321.

Williams, L. A., Parks, G. & Crerar, D. A. (1985). *J. Sediment. Petrol.* **55**, 301–311.

Wrona, T., Jackson, C. A.-L., Huuse, M. & Taylor, K. G. (2015). *Basin Res.* **29**, 556–575.

Wrona, T., Taylor, K. G., Jackson, C. A.-L., Huuse, M., Najorka, J. & Pan, I. (2017). *Geochem. Geophys. Geosyst.* **18**, 1537–1549.